Tropical cyclone cloud-top height and vertical temperature structure detection using GPS radio occultation measurements

Riccardo Biondi,[1,2] Shu-Peng Ho,[3] William Randel,[4] Stig Syndergaard,[5] and Torsten Neubert[1]

[1]   The accurate determination of tropical cyclone (TC) cloud-top height and its vertical thermal structure using the GPS radio occultation (RO) technique is demonstrated in this study. Cloud-top heights are determined by using the bending angle anomaly and the temperature anomaly profiles during the TC events, and the results are compared to near-coincident cloud-top heights determined by Cloud-Aerosol Lidar with Orthogonal Polarization (CALIOP) measurements. Based on 34 closely located RO-CALIOP pairs during 2006 to 2009, TC cloud-top heights from RO are highly correlated with CALIOP ($r = 0.84$), with a mean RO-CALIOP cloud-top height difference of approximately 500 m and a root-mean-square difference near 1 km. GPS RO data also allow analysis of the TC thermal structure, showing warm anomalies in the middle troposphere and cold anomalies in the upper levels, with a strong inversion near cloud top. We further investigate the thermal structure of the TCs from collocated radiosondes, and identify 246 RO-radiosonde pairs from 2001 to 2009. Radiosonde data confirm the thermal structure identified in GPS RO, with a strong inversion near the inferred cloud top. The mean difference between RO-derived inversion heights and those from radiosonde temperature profiles is approximately 500 m. Results show that, while cloud-top height detected from nadir-viewing satellites can be easily biased by a few kilometers, the biases of RO-derived cloud-top height are within ~500 m.

1. Introduction

[2]   Tropical cyclones (TCs) are one of the most destructive natural phenomena. The intensity of a TC is mainly modulated by the magnitude of latent heat released in the cloud system, which is highly correlated with tropical sea surface temperature (SST) [*Emanuel*, 1999]. The strong latent heat released in TCs is also closely related to the organization of convection, three-dimensional moisture distributions, and vertical thermal structure inside and outside the clouds. Because the cloud-top height is linked to the altitude of the temperature and moisture inversion layers, which is closely related to the TC intensity, the accurate determination of the TC cloud-top heights should be useful for monitoring tropical deep convection systems developing into tropical depressions, tropical storms, or hurricanes [*Jensen et al.*, 2005; *Wong and Emanuel*, 2007; *Luo et al.* 2008].

[1]DTU Space, National Space Institute, Copenhagen, Denmark.
[2]The Abdus Salam International Center for Theoretical Physics (ICTP), Trieste, Italy.
[3]UCAR/COSMIC, Boulder, Colorado, USA.
[4]NCAR, National Center for Atmospheric Research, Boulder, Colorado, USA.
[5]DMI, Danish Meteorological Institute, Copenhagen, Denmark.

Corresponding author: R. Biondi, The Abdus Salam International Center for Theoretical Physics (ICTP), Trieste, Italy. (riccardo@biondiriccardo.it)

[3]   In addition, accurate determination of the TC cloud-top heights should help quantify the physical mechanisms that control key atmospheric processes including the radiative budget and the water vapor transport in the upper troposphere and lower stratosphere (UTLS) during the evolution of TCs [*Sherwood et al.*, 2003; *Chaboureau et al.*, 2007; *Grosvenor et al.*, 2007; *Corti et al.*, 2008] and may contribute to monitoring and predicting the development of TCs. For example, a recent theoretical study from *Wong and Emanuel* [2007] demonstrated that the intensity of a mature TC depends on both the SST and the difference of the saturation moist static energy between the eyewall and the undisturbed environment, which are in turn linked to the cloud-top height and cloud-top temperature. *Luo et al.* [2008] has applied cloud-top heights determined by CLOUD SATellite and cloud-top temperatures from Moderate Resolution Imaging Spectroradiometer 11 μm brightness temperatures collocated with hurricanes to *Wong and Emanuel* [2007] method to estimate the hurricane intensity. They confirmed that the derived hurricane intensity has diagnostic skill when compared with those derived from sustained wind speed, SST, and vertical distribution of relative humidity.

[4]   Satellite data are commonly used to determine global cloud-top heights and cloud-top temperatures including those for tropical cyclones over remote oceans [*Prata and Turner*, 1997; *Rozanov et al.*, 2004]. Satellite measurements can also be used to derive key parameters that are directly

related to hurricane track prediction and hurricane intensity estimation. These parameters include the surface temperature, cloud-top temperature, hurricane-center temperature, hurricane-surface pressure gradient, and surface winds at the outer radius [*Dvorak*, 1975; *Kidder et al.*, 1978; *Brueske and Velden*, 2003; *Demuth et al.*, 2004; *Velden et al.*, 2006]. These remote sensing techniques range from active measurements from lidar [*Poole et al.*, 2002] and radar, oxygen A-band technique [*Koelemeijer et al.*, 2002], reflected light polarization [*Knibbe et al.*, 2000], to satellite infrared and microwave sounders and imagers [*King et al.*, 1992]. However, the detected cloud-top heights actually vary dramatically depending on the different physical retrieval methods and satellite spectrum used [*Sherwood et al.*, 2004]. For example, IR atmospheric window (11 μm) brightness temperatures (i.e., usually from meteorological satellites) with either an assumed lapse rate or a lapse rate derived from nearby radiosonde temperature profiles [i.e., *King et al.*, 1992; *Platnick et al.*, 2003; *Rossow and Schiffer*, 1999] are commonly used to determine the cloud-top height. However, the retrieved cloud-top height is highly dependent on the accuracy of the lapse rate derived from the temperature profile, which often has substantial uncertainty [*Naud et al.*, 2002]. The detected cloud-top height from infrared sounding can be as large as 2 km lower when compared with ground-based in situ measurements and collocated lidar measurements [*Minnis et al.*, 2008; *Chang et al.*, 2010]. Using CO_2 slicing retrieval algorithms, temperature sounders, such as Moderate Resolution Imaging Spectroradiometer, the Atmospheric Infrared Sounder, and the Geostationary Operational Environmental Satellite (GOES), are also used to retrieve cloud-top heights. Estimated errors of the derived cloud-top heights can be as large as 3 km, particularly for thin cirrus clouds in the upper troposphere that are semitransparent in the infrared wavelengths [e.g., *Holz et al.*, 2006; *Chang et al.*, 2010]. The most accurate cloud-top heights are obtained from satellite lidar and radar techniques [*McGill et al.*, 2004; *Minnis et al.*, 2008; *Chang et al.*, 2010]. However, their temporal and global coverage are relatively poor compared to that from satellite infrared and microwave sounders.

[5] The objective of this study is to demonstrate the usefulness of GPS radio occultation (RO) measurements to accurately determine cloud-top height for TCs and the vertical temperature structure near the TC cloud top. Using GPS receivers on board low Earth orbit (LEO) satellites, this technique is able to detect the RO phase change of two L-band signals (L1 at 1575.42 MHz and L2 at 1227.60 MHz) crossing the atmosphere, transmitted by a GPS satellite. Because of the vertical variations in the atmospheric refractivity, the signal is refracted and the measurements can be characterized by a total bending angle and corresponding impact parameter by way of the phase change [*Kursinski et al.*, 1997]. Although insensitive to clouds, the high vertical resolution RO measurements are sensitive to the vertical refractivity gradient, which depends on the temperature, pressure, and water vapor distribution. The quality of RO data is consistent at different geographical locations, among different processing centers [*Ho et al.*, 2009a; *Foelsche et al.*, 2011], and among different RO missions [*Ho et al.*, 2009b; *Hajj et al.*, 2004]. The GPS RO technique provides measurements of the atmospheric refractivity with high accuracy, precision, and vertical resolution especially

between 5 and 25 km [*Kursinski et al.*, 1997; *Kuo et al.*, 2004; *Schreiner et al.*, 2007; *Ho et al.*, 2009a, 2009b, 2010, 2012]. The vertical resolution of the GPS RO profiles ranges from about 60 m in the lower troposphere up to 1.5 km in the stratosphere [*Kursinski et al.*, 1997]. *Biondi et al.* [2012] (hereafter Biondi2012) demonstrated that GPS RO data can be used to detect the vertical thermal structures for strong convective systems (CS, defined by cloud-top temperature < 245 K), the convective cluster (CC, defined as the cloud-top temperature < 220 K) and their cloud-top heights. In Biondi2012, the RO-derived cloud-top heights were compared to the adjacent cloud-top heights determined by the lidar measurements from the Cloud-Aerosol Lidar with Orthogonal Polarization (CALIOP) [*Vaughan et al.*, 2004, *Winker et al.*, 2007], which is onboard the Cloud-Aerosol Lidar and Infrared Pathfinder Satellite Observation (CALIPSO). Although there are a few cases in which the cloud-top height differences can be as large as 2 km, they are, in general, less than 1 km. However, it should be noted that the GPS RO measurements and the CALIPSO tracks used in Biondi2012 were never exactly collocated in space and time, which explains part of the differences.

[6] In this study, we examine the feasibility of the RO-cloud height detection method for TC systems, which are characterized by stronger vertical convection and larger horizontal coverage (and possibly with a more complex vertical thermal structure) than the local CS and CC detected by Biondi2012. In Biondi2012, deep convective systems were identified using International Satellite Cloud Climatology Project satellite data. In this study, we collect global TC track information from 2001 to 2009 and obtained from several meteorological centers to clearly identify tracks and radius of TC systems. Using TC track information, we are able to collect RO profiles collocated with TC systems and to analyze the vertical structures and identify the cloud-top heights. GPS RO profiles from multiple RO missions from 2001 to 2009 are collected. The cloud-top heights derived from CALIOP [*Vaughan et al.*, 2004; *Winker et al.*, 2007] total attenuated backscatter are used to verify the RO-derived cloud-top heights. Furthermore, we analyze the thermal structure of the TCs derived from nearby radiosondes (based on 246 near-coincident cases) to validate those derived from RO data.

[7] In section 2 we describe the data sets used for this work, and in section 3 the technique used to detect the cloud-top altitude from GPS RO and the validation methodology. In section 4 we provide examples of RO profiles from which cloud-top heights are determined and compare them with those from near-by CALIOP observations. The thermal structure of the TCs analyzed using the ROs and the collocated radiosonde observations (RAOBs), and the connection between the RO bending angle and the temperature variation, are shown in section 5. The conclusions of the study, the uncertainties of the method, and possible future applications are presented in section 6.

2. Data

[8] 1. GPS RO Data

[9] The fundamental observation of the GPS RO technique is the excess phase (or its time derivative, the Doppler shift) due to the atmosphere as a GPS signal propagates from the GPS transmitter to the LEO receiver [*Kursinski et al.*,

1997]. Assuming local spherical symmetry in the UTLS, the bending angle is converted from the Doppler shift [*Kursinski et al*., 1997; *Ho et al*., 2009a, 2012], and the refractive index as a function of the altitude is derived from the bending angle as a function of the impact parameter using the Abel Transform [*Fjeldbo et al*., 1971]. The refractivity, *N*, related to the refractive index *n*, is defined as

$$N = (n - 1) \cdot 10^6 \qquad (1)$$

[10] Atmospheric refractivity in the neutral atmosphere is dependent on the temperature (*T* in Kelvin), pressure (*p* in millibar), and water vapor pressure (*e* in millibar) [*Smith and Wientraub*, 1953]

$$N = 77.6 \frac{p}{T} + 3.73 \cdot 10^5 \frac{e}{T^2} \qquad (2)$$

Because the water vapor amount in the UTLS is very small (and negligible in equation (2)), the refractivity at these altitudes is mainly a function of pressure and temperature. The GPS RO data were downloaded from the Constellation Observing System for Meteorology, Ionosphere, and Climate (COSMIC) Data Analysis and Archive Center (CDAAC) website (http://cosmic-io.cosmic.ucar.edu/cdaac/index.html). RO profiles were collected from CHAllenging Minisatellite Payload (CHAMP, from 2001 to 2008) [*Wickert et al*., 2001], COSMIC (launched in April 2006) [*Anthes et al*., 2008], Gravity Recovery And Climate Experiment (GRACE, launched in 2004) [*Beyerle et al*., 2005], and Satélite de Aplicaciones Científicas-C (launched in 2000) [*Hajj et al*., 2004]. For this work, as in Biondi2012, we use the raw unoptimized bending angle from the level 2 atmospheric profiles (CDAAC atmPrf product) and the temperature from the level 2 wet profiles (CDAAC wetPrf product) to detect the TC cloud-top height and analyze the corresponding thermal structure. All the parameters are reported as a function of the geometric height above the mean sea level and the location of the tangent points. More details about the GPS RO data and the CDAAC products used in this study can be found in Biondi2012.

[11] 2. TC tracks and cloud measurements

[12] Tropical cyclone track information (TC best tracks) is collected from several meteorological centers. The global cloudy scenes are identified by using the brightness temperatures from the GOES, Meteorological SATellite 1 (MTSAT-1), and Geostationary Meteorological Satellite (GMS), whereas the World Wide Lightning Location Network (WWLLN) data set is used to identify convection activity. The cloud-top height is determined by CALIOP and is also derived from the temperature profiles from adjacent radiosonde measurements (see below).

[13] 1. TC track information

[14] The TC track information is collected from different institutes, which include (i) the U. S. National Hurricane Center (for the Atlantic, Caribbean and Eastern Pacific oceans); (ii) the Australian Government Bureau of Meteorology (for the Western, Northern and Eastern Australia regions); (iii) the Japan Meteorological Agency (for the Western and Northern Pacific oceans); (iv) the Météo France (for the South-West Indian basin); and (v) the Unysis Weather (for the Northern Indian Ocean, Bay of Bengal

and Arabian Sea). The following TC information is collected: the name, dates, coordinates, intensity, and minimum pressure of the storm at least every 6 h during the formation of the tropical cyclone. Based on in situ and satellite measurements, these are basically postcyclone analyses [*Jarvinen et al*., 1984], which track each stage of the TC development (i.e., the tropical depression, the tropical storm, hurricane/typhoon, and the extra-tropical cyclone). During the Hurricane Hunters missions or other specific campaigns, additional information, such as: eye dimension, storm direction, and speed, is also available [*Aberson et al*., 2006]. In this study, TC information on location, time, and radius of the TC, is used to identify the collocated GPS ROs (see section 3).

[15] 2. Cloudy scenes identified by GOES measurements

[16] The GOES brightness temperatures (BT) are analyzed near the location of the RO profiles to identify cloudy scenes during TCs in the Atlantic and East Pacific basins. The GOES VARiable IMaGer data were downloaded from the Comprehensive Large Array Data Stewardship System. The GOES VARiable IMaGer data are GOES11 and GOES12 at 6.8 μm (band 3) and 10.7 μm (band 4). The BT differences between the GOES 10.7 μm channel (window channel) and the 6.8 μm channel (water vapor channel) are used to determine the cloudiness. In clear sky and low-level cloud conditions, the BT for the water vapor channel is smaller than that for the window channel. For high clouds, the BT for the water vapor channel is larger than that for the window channel [*Schmetz et al*., 1997; *Chaboureau et al*., 2007].

[17] 3. Cloudy scenes identified by MTSAT-1 and GMS measurements

[18] The MTSAT-1 images from Japan Meteorological Agency and the GMS images from Japan Aerospace Exploration Agency were used to detect the cloudiness during TCs over the Pacific Ocean. Like GOES data, MTSAT-1 and GMS BT in the water vapor channel (6.5 μm) and window channel (11 μm) are used to determine general cloud scenes during the TCs.

[19] 4. The Proxy for Convection activity identified by the WWLLN data set

[20] Together with GOES BTs, the WWLLN data set [*Rodger et al*., 2005] is used as proxy for convection activity in the same area (see section 4).

[21] 5. TC cloud height detection from CALIOP

[22] On board the CALIPSO satellite, CALIOP is a two-wavelength (532 and 1064 nm) polarization-sensitive lidar that provides high-resolution vertical profiles of aerosols and clouds [*Vaughan et al*., 2004; *Winker et al*., 2007]. Launched in April 2006, the CALIOP has a 70 m nominal footprint with vertical resolution ranging from 30 m below 8.2 km altitude to 180 m above 20.2 km altitude. The CALIOP data products are available from the beginning of June 2006. With high vertical resolution, the CALIOP is able to detect optically thin cirrus clouds (with optical thickness down to 0.01) and geometrically thin aerosol layers. The cloud-top layer determined by CALIOP is consistent with those derived from in situ measurements [*McGill et al*., 2007]. In this study, the cloud-top heights derived from CALIOP level 1 total attenuated backscatter products (CAL_LID_L1, version V03) are used to validate the RO-derived TC cloud-top heights.

[23] 6. Thermal structure derived from radiosondes

[24] The radiosonde temperature and moisture profiles are archived from the National Center for Atmospheric Research
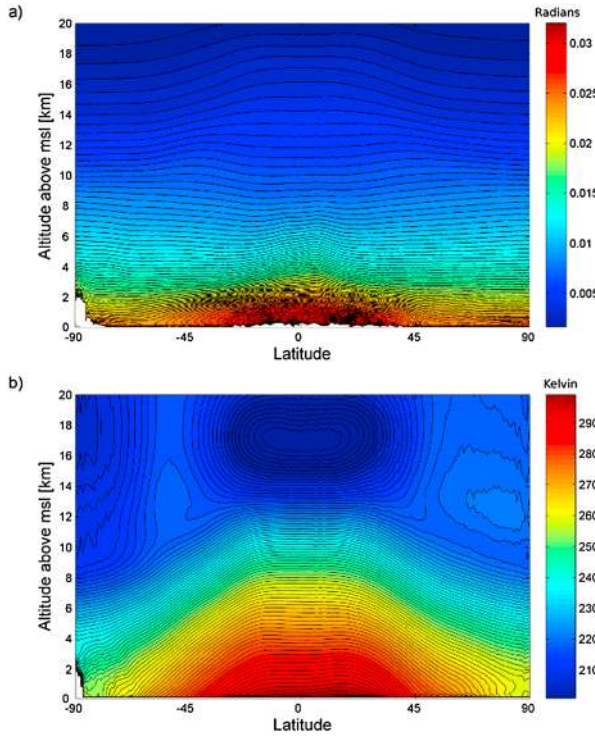
Figure 1. (a) Bending angle climatology latitudinal dependency and (b) temperature climatology latitudinal dependency. The climatologies are displayed from the surface to 20 km altitude.

mass store (data set 353.4). The radiosonde temperature profiles are used to derive the thermal structure during TC events, and the upper level inversions (likely associated with cloud-top heights) are compared to those derived from the collocated RO profiles. These operational radiosonde data are typically available every 6 h and are reported at mandatory levels (1000, 925, 850, 700, 500, 400, 300, 250, 200, 150, 100, 70, 50, 30, 20, and 10 hPa). Radiosonde data from 2001 to 2009 are used in this study.

3. GPS RO TC Cloud-Top Height Detection Method

[25] Cloud-top heights are calculated using the anomalies of the high-resolution GPS RO bending angle profiles near the TCs relative to a bending angle climatology. In addition, the vertical thermal structures during TCs are calculated relative to a temperature climatology. The procedure consists of the following steps:

[26] Step 1: Vertical interpolation: All the atmPrf bending angle and wetPrf temperature profiles are first interpolated to a 50 m vertical sampling grid.

[27] Step 2: Generation of global bending angle and temperature background climatology: Using GPS RO data from 2001 to 2009 collected from CDAAC, all the available multiyear bending angle profiles and temperature profiles are binned into a $1° \times 1°$ grid. To obtain enough RO samples to compute the representative mean state of the bending angle in each of the $1° \times 1°$ grids, we construct the multiyear mean climatology (independent of month or season). The $1° \times 1°$ grids provide about 150 km box-diagonal distance

in equator but will provide higher box-diagonal distance in higher latitudes, which is more compatible to the horizontal resolution for RO data. Although not shown, the RO-derived cloud-top heights are nearly identical when different (e.g., $2.5° \times 2.5°$ grids) grid sizes are used. Figure 1 depicts the climatological structure of mean bending angle and the mean temperature profile, reproducing well-known behavior.

[28] Step 3: Collocation of RO, TC events, CALIOP, and identification of cloudiness: Using TC tracks and satellite images from GOES and GMS, the temporal and spatial differences between the center of TC events and available RO data can be identified. BT differences between the GOES water vapor channel (6.8 μm) and window channel (10.8 μm) are used to determine both clear and low cloud conditions (BT (6.8) − BT (10.8) < 0) and high cloud conditions (BT (6.8) − BT (10.8) > 0) [*Schmetz et al.*, 1997; *Chaboureau et al.*, 2007]. All the selected cases are then compared with the CALIPSO ground track time and location. From 2006 (launch of CALIPSO) to 2009, we identified 34 collocated GPS ROs and CALIOP measurements during TC events, based on coincidence within 3 h and 200 km (see Table 1).

[29] Step 4: Computation of the bending angle anomaly during the TCs: To identify the cloud-top height during a

Table 1. Tropical Cyclones Colocated With GPS RO and CALIOP[a]

Tropical Cyclone	Distance (km)	Time Difference (min)	Basin
RUMBIA 2006	**27**	**92**	**West Pacific**
ALBERTO 2006	**27**	**119**	**Atlantic**
KRISTY 2006	**18**	**96**	**East Pacific**
PEIPAH 2007	**60**	**7**	**West Pacific**
PABUK 2007	**15**	**52**	**West Pacific**
MAN-YI 2007	**92**	**66**	**West Pacific**
KROSA 2007	**18**	**39**	**West Pacific**
PABUK 2007	**79**	**58**	**West Pacific**
NAKRI 2008	**84**	**85**	**West Pacific**
HANNA 2008	**58**	**37**	**Atlantic**
PHANFONE 2002	**20**	**88**	**West Pacific**
ELIDA 2008	**3**	**102**	**East Pacific**
LOWELL 2002	**47**	**54**	**East Pacific**
WUTIP 2007	111	19	East Pacific
SIDR 2007	106	2	Indian Ocean
PABUK 2007	169	39	East Pacific
HANNA 2008	110	4	Atlantic
BAVI 2008	104	55	East Pacific
EDOUARD 2008	113	18	Atlantic
NURI 2008	108	18	East Pacific
FLORENCE 2006	75	157	Atlantic
HELENE 2006	44	135	Atlantic
WUKONG 2006	37	115	East Pacific
INGRID 2007	57	158	Atlantic
WIPHA 2007	81	127	East Pacific
USAGI 2007	18	177	East Pacific
MELISSA 2007	90	130	Atlantic
KROSA 2007	34	136	East Pacific
NOEL 2007	53	149	Atlantic
ERIN 2007	62	156	Atlantic
EDOUARD 2008	63	130	Atlantic
KAMMURI 2008	99	120	East Pacific
OMAR 2008	97	125	Atlantic
EDOUARD 2008	47	166	Atlantic

[a]Time (in minute) and location (in km) differences between colocated GPS ROs and CALIPSO during the TC events. The distance is referring to the GPS RO tangent point at 16 km altitude and the closest CALIPSO track. In bold the closest cases within 2 h and 100 km.
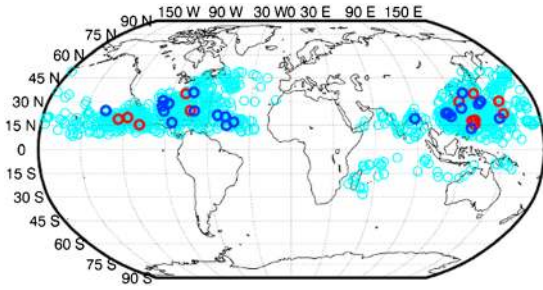
Figure 2. Locations of the tropical cyclones colocated with the GPS radio occultations (1194). In dark blue all the cases also colocated with CALIOP (34) and in red the closest (13) in a time window of 2 h and space window of 100 km.

TC, we compute the fractional bending angle anomaly relative to the climatology during the TC as

$$\alpha_{\text{anomaly}}(i) = 100 \cdot \frac{\alpha_{\text{TC}}(i) - \alpha_{\text{C lim}}(i)}{\alpha_{\text{C lim}}(i)} \quad (3)$$

where i is the index of the altitude level (every 50 m from the surface to 20 km), α_{TC} is the bending angle profile during the TC, and α_{Clim} is the bending angle climatology at the location of the RO. Because bending angle decreases exponentially with height, we examine the bending angle anomalies in a fractional sense. The bending angle anomalies in the UTLS during the TCs relative to the climatology are related to the vertical distribution of the density anomaly perturbed by the TCs relative to the mean atmosphere. The height of the lowest local maximum of α_{anomaly} in the UTLS, is defined as TC cloud-top height (termed $RO_{\text{B\_top}}$). A variation of at least 3% of bending angle anomaly over 2 km of altitude is required to define the local maximum height as $RO_{\text{B\_top}}$.

[30] Step 5: Computation of the corresponding temperature anomalies during the TCs: To quantify the vertical temperature perturbed during the TCs, we also compute the vertical distribution of the temperature anomaly relative to the mean atmosphere using the following equation:

$$T_{\text{anomaly}}(i) = T_{\text{TC}}(i) - T_{\text{C lim}}(i) \quad (4)$$

where i is the index of the altitude levels (every 50 m from the surface to 20 km), T_{TC} is the temperature profile during the TCs, and T_{Clim} is the temperature climatology. T_{anomaly} is used to relate temperature and bending angle variations and to study the vertical thermal structure during the TCs. The height of the lowest local minimum of T_{anomaly} in the UTLS (termed $RO_{\text{T\_top}}$) is defined as the TC cloud-top height based on the temperature anomaly. A variation of at least 1 K of temperature anomaly over 2 km of altitude is required to define the local minimum height as $RO_{\text{T\_top}}$. As shown later, $RO_{\text{T\_top}}$ derived from all the collected cases are close to, but not exactly equal to $RO_{\text{B\_top}}$ (see below).

4. Comparisons of Cloud-Top Heights From RO With Collocated CALIOP

[31] Collocated with the tropical cyclone best tracks in a time window of 3 h, we have identified about 1200 RO profiles (Figure 2) from different radio occultation missions

(namely, Satélite de Aplicaciones Científicas-C, CHAMP, COSMIC, and GRACE) from 2001 to 2009. These profiles are distributed mainly in the eastern and western Pacific basins, and the western Atlantic basin. Among these 1200 profiles, we further identified 34 TC events where the RO profiles are collocated with CALIOP within 3 h and 200 km during the period from 2006 to 2009 (Table 1, blue and red circles in Figure 2; the red circles are for the RO-CALIOP pairs within 2 h and 100 km). In this section, we apply the TC height detection method to the RO data when they are collocated with CALIOP. Case studies of two tropical cyclones, the typhoon Krosa and the typhoon Nakri, are presented.

4.1. Typhoon Krosa 2007

[32] Typhoon Krosa was a tropical cyclone in the western Pacific basin, which began as a tropical depression on 1 October 2007, strengthened to a peak intensity of 105 kts (10 min average) on 5 October and made landfall on northeastern Taiwan on 6 October, after which it dissipated. On 2 October it was a tropical storm with the center located at 16.5°N and 131.5°E. In Figure 3, the water vapor BT from GMS illustrates the moisture structure of Krosa on 2 October. The storm had a maximum sustained wind speed of 55 kts and a minimum pressure of 990 hPa. A GPS RO occurred on 2 October at 3.42 UTC in a rainband (Figure 3a
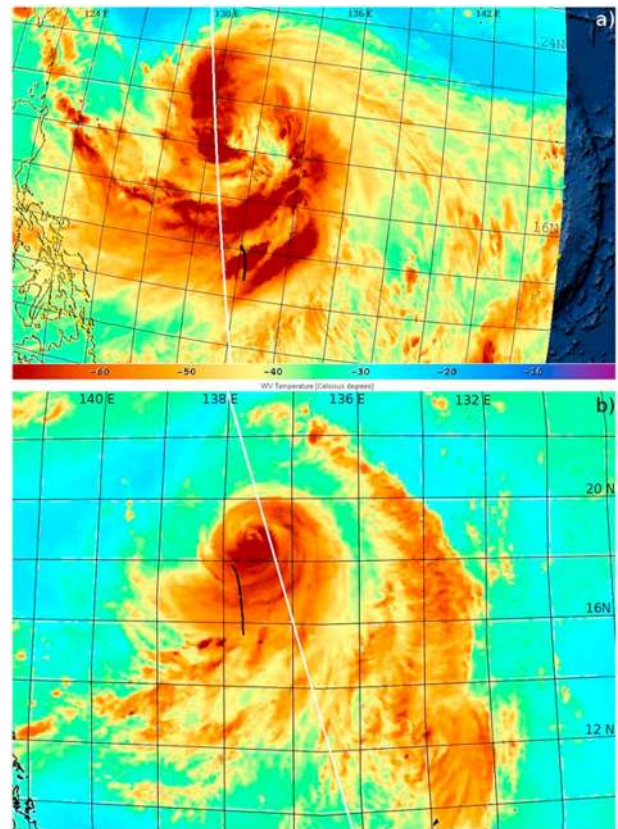

Figure 3. Structure of Krosa (top) on 2 October 2007. Structure of Nakri (bottom) on 31 May 2008. Colors denote GMS brightness temperature (° Celsius) in the water vapor channel (6.5 μm), with brown denoting low values. The black line denotes the GPS RO tangent points and the white line is the CALIPSO track.
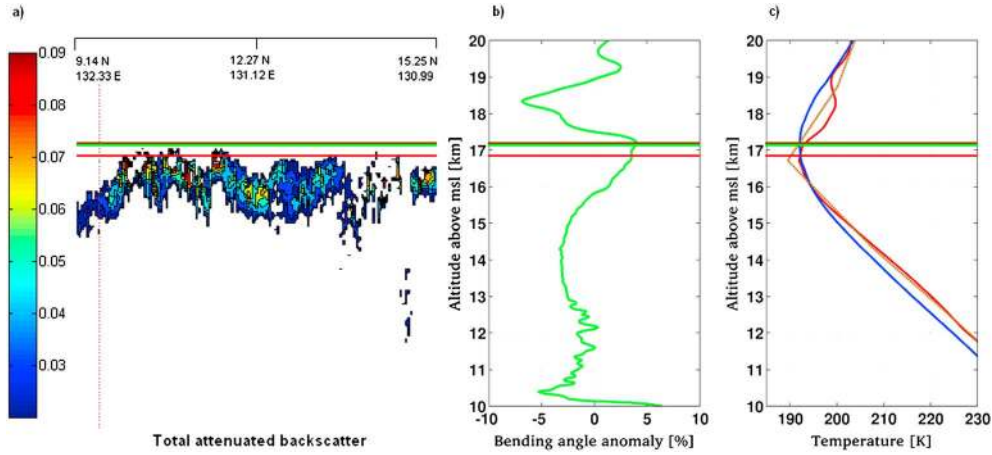
Figure 4. Typhoon Krosa, 2 October 2007. (a) Total attenuated backscatter at 532 nm from CALIOP, (b) RO bending angle anomaly profile, and (c) three different temperature profiles. The three different temperature profiles are from the RO (red), from the ECMWF model (brown), and the mean climatological profile (blue). The horizontal red line marks the altitude of the coldest point of the RO profile, the horizontal green line marks the altitude of the maximum in the bending angle anomaly, and the horizontal brown line marks the altitude of the coldest point in the climatological profile.

shows the tangent point trajectory as a black line), and CALIPSO overpassed the storm at 4.50 UTC (Figure 3a, white line), about 60 km west of the RO tangent points. Between 3.30 and 4.30 UTC more than 1500 strokes were detected from the WWLLN within a distance of 200 km from the GPS RO tangent point (not shown).

[33] Figure 4 depicts the GPS RO bending angle anomaly profile and the temperature vertical profile at 3.42 UTC. In general, the height of the lowest local maximum of bending angle anomaly is very close to that of the lowest temperature minimum (Figure 4), which is usually the same as the height of the lowest local minimum in the temperature anomaly (not shown). Figure 4 shows that the bending angle anomaly profile (central panel) exhibits two local maxima in the UTLS. The

lower maximum is at 17.1 km altitude (green horizontal line), about 300 m above the altitude of the coldest point (192 K) in the RO temperature profile (red horizontal line at 16.8 km altitude, right panel of Figure 4). The second maximum in the bending angle anomaly profile is above 19 km, corresponding to a second temperature minimum at 199 K. The corresponding temperature climatology is shown as a blue line in the right panel of Figure 4, whereas the temperature profile from European Centre for Medium-Range Weather Forecasts (ECMWF) interpolated to the RO location (downloaded from CDAAC), is shown as the yellow curve. The maximum altitude of the cloud top detected by CALIOP is at 16.8 km (Figure 4, left panel), 300 m below the altitude of the lower bending angle maximum.
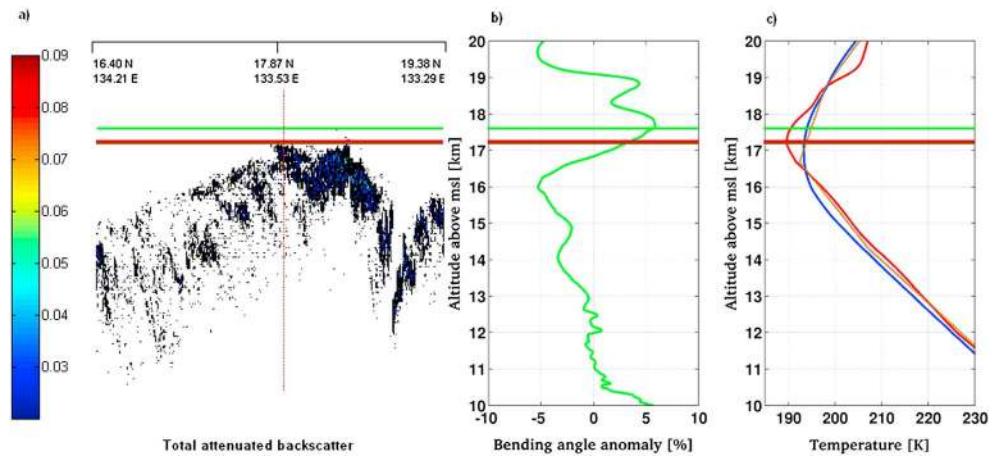

Figure 5. Typhoon Nakri, 31 May 2008. (a) Total attenuated backscatter at 532 nm from CALIOP, (b) RO bending angle anomaly profile, and (c) three different temperature profiles. The three different temperature profiles are from the RO (red), from the ECMWF model (brown), and the mean climatological profile (blue). The horizontal red line marks the altitude of the coldest point of the RO profile, the horizontal green line marks the altitude of the maximum in the bending angle anomaly, and the horizontal brown line marks the altitude of the coldest point in the climatological profile.
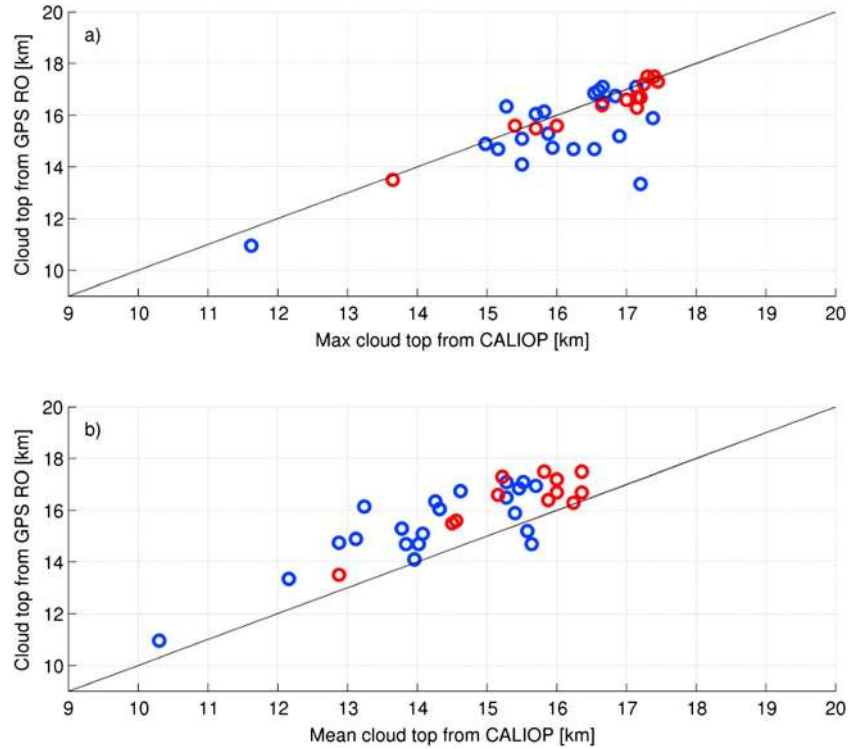
Figure 6. Scatter plot between the cloud top from CALIOP and from GPS ROs, the red circles are the 13 cases closest in time and space (2 h and 100 km). (a) Related to the highest top of the system and (b) with the averaged top of the system. Mean bias, RMSE and correlations are reported in Table 2.

4.2. Typhoon Nakri 2008

[34] Typhoon Nakri was a tropical cyclone in the Western Pacific basin which began as a tropical depression on 26 May 2008, strengthened to a peak intensity of 100 kts (10 min average) and a minimum pressure of 930 hPa on 29 May. On 31 May the center was located at 18.8°N and 132.8°E, with a maximum sustained wind speed of 75 Kt and a minimum pressure of 965 hPa. A GPS RO occurred on 31 May at 3.15 UTC about 100 km from the center (Figure 3b shows the tangent point trajectory as a black line), and CALIPSO passed over the storm at 4.40 UTC about 80 km from the RO tangent points (Figure 3b, white line). Within 1 h from the GPS RO, the WWLLN data set shows 50 strokes less than 200 km from the GPS RO tangent points (not shown).

[35] Figure 5 depicts the GPS RO bending angle anomaly profile and temperature vertical profile at 3.15 UTC. The bending angle anomaly (central panel) has a local maximum at 17.6 km altitude, 300 m above the coldest point of 189.7 K in the RO temperature profile (right panel). The CALIOP attenuated backscatter (left panel) shows the maximum cloud-top altitude at 17.1 km and an averaged storm cloud top at about 16 km altitude.

4.3. Statistical Comparisons of Cloud-Top Heights From RO and Collocated CALIOP

[36] Comparison of cloud-top heights detected by RO with CALIOP measurements for all 34 cases, are shown in Figure 6. Within this data set, we further selected different subsets depending on the time/space distance between the GPS RO tangent points and the CALIOP tracks, including 13 cases with coincidences within 2 h and 100 km. Table 2 shows the mean bias (RO minus CALIOP maximum cloud-top height), root-mean-square error (RMSE), and correlation for the full data set of 34 cases and for each of the subsets. For all of the 34 cases, the correlation coefficient is equal to 0.84, while it is equal to 0.97 for the RO-CALIOP pairs that are as close as 2 h and 100 km (13 cases). The mean difference between RO and CALIOP maximum cloud-top

Table 2. Colocation Statistics[a]

	# Cases	Mean Bias (km)		RMSE (km)		Correlation	
		Max Top	Mean Top	Max Top	Mean Top	Max Top	Mean Top
Time 3 h Space 200 km	34	−0.46	1.11	1.00	1.35	0.84	0.77
Time 2 h Space 200 km	20	−0.45	0.80	0.78	1.05	0.82	0.79
Time 3 h Space 100 km	27	−0.35	1.29	0.92	1.44	0.81	0.90
Time 2 h Space 100 km	13	−0.22	0.99	0.36	1.12	0.97	0.93

[a]Mean bias, RMSE, and correlation of cloud top altitudes from ROs (computed with the bending angle anomaly, RO_{B_top}) and CALIPSO during TCs using different time/space windows. Max top is related to the maximum cloud top derived from CALIOP measurements; mean top is related to the mean cloud top derived from CALIOP measurements.
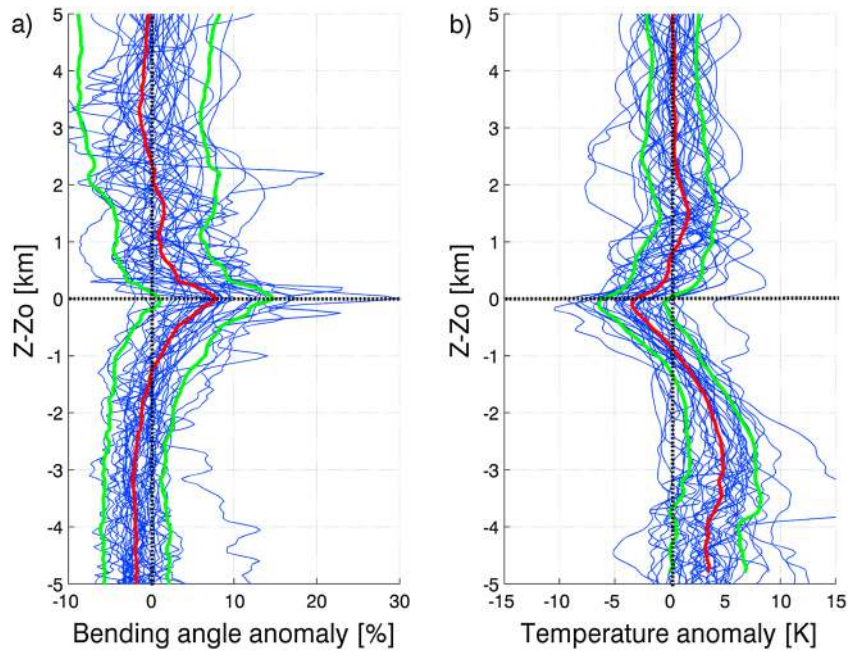
Figure 7. Vertical profiles of the GPS RO (a) bending angle anomalies and (b) temperature anomalies, calculated with respect to the altitude of the cloud top (Zo) derived from CALIOP measurements. Each of the 34 cases is shown in blue, the average in red, and the average ± one standard deviation in green.

height is 457 m with an RMSE of 996 m. For those 13 RO-CALIOP pairs that are less than 2 h and within 100 km, their mean difference (for the CALIOP maximum cloud top) is equal to 223 m with an RMSE of 365 m.

[37] Because of the temporal and spatial mismatches between the RO tangent points and CALIPSO tracks, we also compare the estimated RO cloud-top altitude with the storm-averaged cloud-top altitude along the CALIOP tracks. For computation of the storm-averaged cloud-top altitude, we average the altitudes of the cloud tops along a 200 km piece of the CALIOP track (occasionally shorter if the cloud-top altitude drops down by 8 km over 100 km, which is used as an indication that the track is no longer inside the TC) using the point of closest approach to the RO tangent point (the one at 16 km altitude) as the midpoint. In this case the correlation coefficient is still high (0.77), especially for the 13 cases within 2 h and 100 km (0.93), but a bias of approximately 1 km is evident (cf. Figure 6 and Table 2). In general, the RO-derived cloud-top heights are much closer to the maximum cloud-top height from CALIOP than those of mean cloud-top height (Table 2).

[38] To further compare the cloud-top heights derived from bending angle and temperature profiles, Figure 7 depicts the vertical distribution of the bending angle and the temperature anomalies relative to the maximum cloud-top altitude derived from CALIOP for all of the 34 cases. In general, below the CALIOP cloud top (from −5 km to −2 km in Figure 7), the troposphere is, on average, warmer (Figure 7b, about 4 K) than the climatology consistent with previous observations of the TC [Merrill, 1991; Kidder et al., 2000]. Correspondingly, the mean bending angle anomaly (Figure 7a) is negative. Approaching the cloud top (from −2 km to 0 km in Figure 7), the mean bending angle anomaly increases rapidly, becoming positive and reaching the maximum amplitude exactly at the cloud-top

heights identified by CALIOP. The temperature is nearly 5 K colder than the climatology at the same height. Above the cloud top (~2 km in Figure 7), there is not any significant variation in bending angle and temperature relative to their corresponding climatologies.

[39] For all 34 RO-CALIOP cases analyzed in this study, the bending angle anomalies show local maxima in the UTLS (often corresponding to the coldest point in the temperature profile), and in some cases there are two local maxima in the UTLS for bending angle anomalies and correspondingly two local minima for temperature anomalies (i.e., for TC Krosa in Figure 4). The presence of two local maxima in the bending angle anomalies (and two local minima in the temperature anomalies) is common for strong convective systems where the cloud tops are lower than the tropopause heights [Biondi et al., 2012]. In these cases, the lower bending angle maximum corresponds to the cloud-top altitude and the higher maximum usually corresponds to the tropopause height. When the TC top reaches the tropopause, the tropopause is lifted up by the convection [Romps and Kuang, 2009] creating the second temperature minimum.
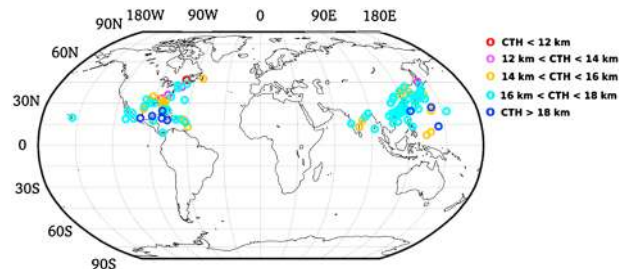

Figure 8. Global distribution of colocated GPS ROs and RAOBs during TCs depending on the cloud-top height altitude.
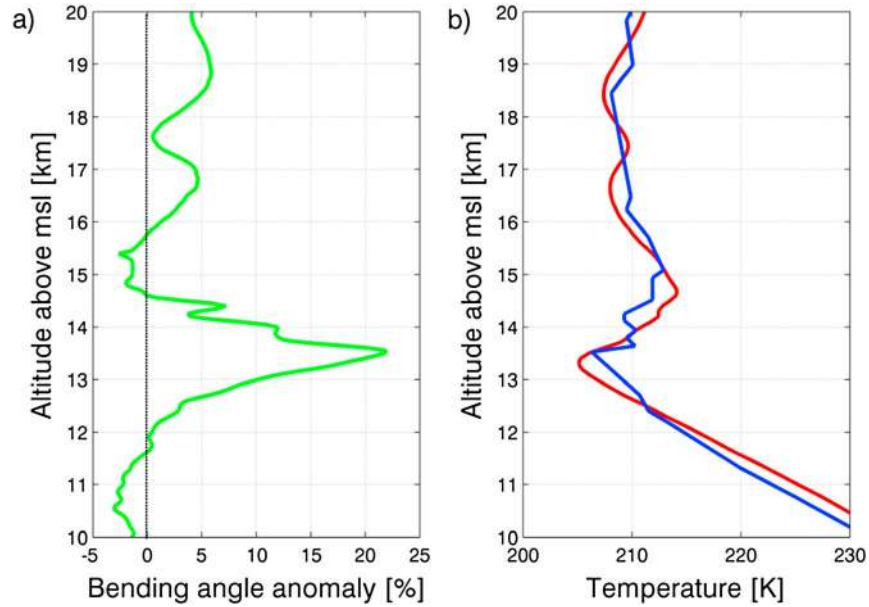
Figure 9. Tropical Depression One 2009, 29 May in the Atlantic basin. (a) Bending angle anomaly profile and (b) temperature profiles from co-located GPS RO (red) and RAOB (blue).

5. Comparisons of Thermal Structure From RO and Collocated Radiosondes

[40] To extend the validation, among the 1200 RO profiles collocated with the TC best tracks in a time window of 3 h (Figure 2), we further identify RO profiles collocated with available radiosonde (RAOB) data within 6 h and 400 km. Only RAOB profiles reaching the UTLS around 20 km altitude are used. The collocated RO-RAOB pairs are mainly distributed near the western coast of the Pacific and Atlantic oceans (Figure 8). In total 246 collocated RO-RAOB pairs from 2001 to 2009 were found, and our results are based on these 246 pairs.

[41] Because the radius of a midsized hurricane is about 3 to 6° of latitude (300–600 km), the RO-RAOB pairs within 6 h and 400 km should still be reasonably covered by the same TC system. Figure 9 depicts the RO vertical bending angle anomaly and the corresponding RO and RAOB temperature profiles when they are collocated with Tropical Depression One 29 May 2009 in the Atlantic basin. The distance between the RO tangent point (occurred at 2.59 UTC) and the center of Tropical Depression One (located at 38°N and 68.6°W) is about 100 km, while the collocated RAOB (Chatham, MA—sonde ID 74494) is about 200 km away from the RO profile. Figure 9 shows a strong bending angle anomaly at about 13.5 km altitude, corresponding to a temperature minimum (at about 13.3 km) and an inversion layer observed by both GPS RO and ROAB. Based on the comparisons with CALIOP shown previously, this inversion layer is likely collocated with the cloud top of the TC, so that the inversion layer can identify the cloud top.

[42] Applying the RAOB temperature profiles to the RO cloud-top height detection method introduced in section 3 (equation (4) and variation of at least 1 K of temperature anomaly over 2 km of altitude), and using the GPS RO temperature climatology as reference, we computed the cloud tops for all of the 246 cases (termed $RAOB_{T\_top}$) and we compared them to the RO_{B_top} and the RO_{T_top}. Using the $RAOB_{T\_top}$ method, several cases are excluded from the analyses because clear temperature anomalies are not evident (the condition of temperature anomaly variation of at least 1 K over 2 km of altitude is not satisfied possibly related to the coarse vertical resolution of the RAOB measurements) so that the number of samples decreases to 183 (i.e., a clear cloud top could not be identified in approximately 25% of the 246 cases). Figure 10 shows that the RO_{B_top} from 9 to 19 km are, in general, consistent with those derived from RAOB temperature profiles (i.e., $RAOB_{T\_top}$). The red circles in Figure 10 are for the RO-RAOB pairs within 4 h and 300 km. Comparing all of the 183 cases (Figure 10, blue and red circles), the correlation coefficient is 0.72, and
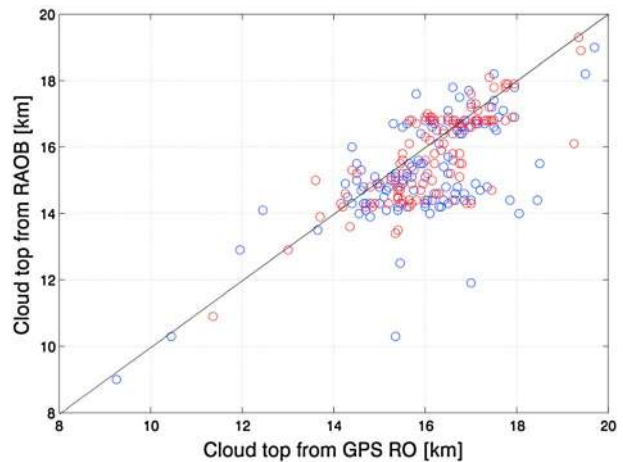

Figure 10. Scatter plot of the cloud top heights from RAOBs versus those from GPS ROs (within 6 h and 400 km of each other). The red circles are 113 cases where the RAOBs and ROs are closest in time and space (within 4 h and 300 km).
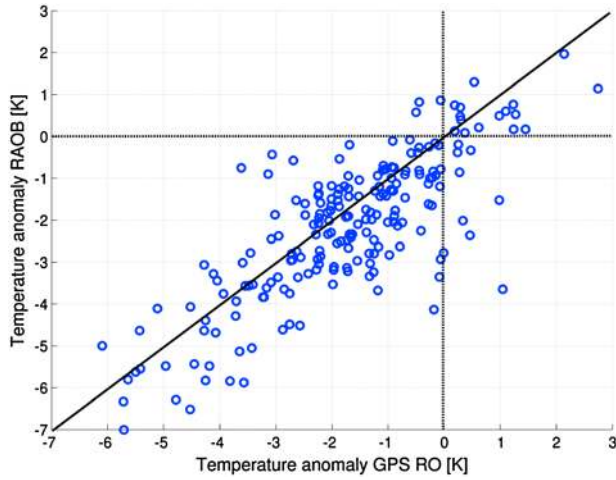
Figure 11. Scatter plot comparing the temperature anomaly from the GPS RO with that of the RAOB at the cloud-top altitude (cloud-top altitude computed using the RAOB temperature anomaly).

the mean difference between RO_{B_top} and $RAOB_{T\_top}$ is 562 m with a root mean square error of 1.23 km. Excluding the cases with a spatial distance larger than 300 km and a temporal delay longer than 4 h, we obtain 113 cases (Figure 10, red circles) with a correlation coefficient of 0.81. The mean difference between RO_{B_top} and $RAOB_{T\_top}$ is now about 400 m with a root mean square error of 1.02 km. For the most part, RO_{B_top} and $RAOB_{T\_top}$ are between 14 and 18 km altitude and those RO-RAOB pairs are mainly distributed between 15° N and 30°N (Figure 8). Figure 8 displays the RO_{B_top} ranges in different colors. In general, the RO_{B_top} distribution is consistent with the SST distribution where the high RO_{B_top} is mainly over the tropics and lower RO_{B_top} is mainly over higher latitudes.

Cases with relatively large differences between RO_{B_top} and $RAOB_{T\_top}$ are possibly due to temporal and spatial mismatches of the RO-RAOB pairs, to the large footprint of RO and RAOB and/or the limited vertical resolution of RAOB profiles.

[43] Figure 11 compares the RO and the RAOB temperature anomalies at the $RAOB_{T\_top}$ for all the 183 cases collocated within 400 km and 6 h. This is to further quantify how the uncertainties of RO-RAOB cloud-top heights are related to the RO and the RAOB temperature anomalies. The temperature anomalies are computed using equation (4), whereas the wetPrf temperature climatology is used as reference. The difference of the RO temperature anomalies and RAOB temperature anomalies relative to the temperature climatology are typically within 1–2 K in Figure 11. For the RO-RAOB temperature anomaly pairs in Figure 11, the correlation coefficient is 0.79. The mean difference between RO and the RAOB temperature anomalies at the RO_{B_top} is 0.38 K, and a standard deviation relative to the mean bias of 1.03 K.

[44] Figure 12 depicts the vertical profiles of the mean bending angle anomaly from the GPS RO (Figure 12a) and the mean temperature anomaly from the GPS RO (Figure 12b) calculated with respect to the cloud-top altitude from GPS RO bending angle (RO_{B_top}), and the mean temperature anomaly from the RAOB (Figure 12c) calculated with respect to the cloud-top altitude from RAOB temperature ($RAOB_{T\_top}$) for all 183 collocated events. The RO anomaly statistics (here for more than 200 profiles) shows basically the same behavior as the statistics for the 34 RO profiles in Figure 7. The RAOB temperature anomaly statistics (for 183 cases) show a similar behavior as the RO temperature anomaly statistics, although the structure is slightly smoother. In the troposphere below the cloud top (from −5 km to −2 km of altitude), the bending angle anomaly is negative, and the temperature
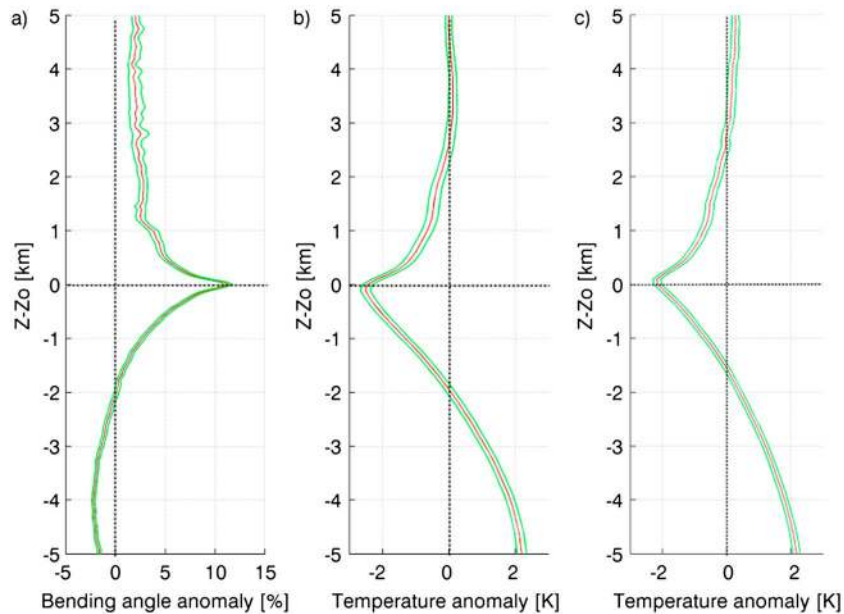

Figure 12. (a) Vertical profile of the GPS bending angle anomaly, (b) the temperature anomaly from GPS RO, and (c) the temperature anomaly from RAOB, calculated with respect to the altitude of the cloud top (Zo). The red curve is the average and the green curves are the mean ± the standard deviation of the mean.
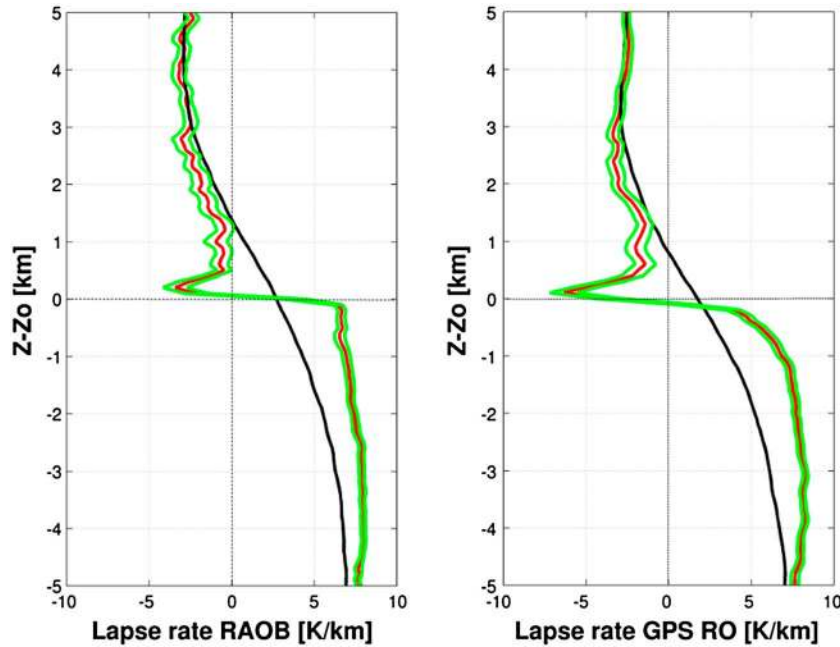
Figure 13. Vertical profile of the RAOB-derived temperature lapse rate $(-dT/dz)$ (a) with respect to the altitude of the cloud top computed from the RAOB temperature anomaly and GPS RO-derived temperature lapse rate and (b) with respect to the altitude of the cloud top computed from the variation of bending angle anomaly. The red curve is the TC average, the green curves are the average $\pm$ the standard deviation of the mean and the black curve is the averaged climatological lapse rate.

is warmer than the climatology. Near RO_{B_top} the temperature is colder than the climatology. Above RO_{B_top} both the bending angle and the temperature profiles are gradually approaching the background values. This is consistent with the results shown by the 13 RO-CALIOP pairs (section 4.3).

[45] Figure 13 compares the lapse rate $(-dT/dz)$ structure during TC events with the climatological lapse rate for RAOB profiles (Figure 13a) with respect to the altitude of the cloud top computed from the RAOB temperature anomaly and for RO profiles (Figure 13b) with respect to the altitude of the cloud top computed from the RO bending angle anomaly. Below the cloud-top height both RAOBs and ROs, show a difference between the lapse rate during the TCs which is 2–3 K/km larger than the climatological value. Above the cloud the lapse rate from ROs becomes negative with an averaged amplitude reaching −3 K/km.

6. Summary and Discussions

[46] In this study, we have demonstrated the usefulness of GPS RO bending angle anomalies and temperature anomalies to identify the cloud-top height of TCs. Although the propagation of GPS signals is not sensitive to clouds, the high vertical resolution RO data are very sensitive to vertical atmospheric temperature gradients associated with TCs, which we show are related to cloud-top heights determined by the lidar measurements from CALIOP. Based on 34 collocated RO-CALIOP pairs available from 2006 to 2009, the RO-derived cloud-top height for TCs are highly correlated $(r = 0.84)$ with those from CALIOP, especially when they are close in time and space $(r = 0.97$ for collocations

within 1 h and 200 km). The mean RO-CALIOP cloud-top height difference is equal to 457 m with a root mean square error of 996 m. The RO bending angle anomalies are linked to sharp temperature inversions near the cloud-top altitude. Furthermore, we identified 246 RO-RAOB pairs close to TCs from 2001 to 2009, which are within 6 h and 400 km. Both the RO and RAOB measurements identify a temperature inversion layer, which are likely associated with the TC cloud top. Although the RAOBs do not observe clouds directly, their good agreement with RO thermal structure (which have been compared with CALIOP cloud-top heights) suggests the RAOB inversion layers can be used as a proxy for the TC cloud-top altitude. The mean difference between RO-derived cloud-top heights and those derived from RAOB temperature profiles were found to be 562 m with a root-mean-square error of 1.23 km. Based on our samples of the 34 RO-CALIOP pairs and the 246 RO-RAOB pairs, almost each individual anomaly profile pair shows a similar variation of the bending angle and temperature anomalies: the positive bending angle anomalies are closely associated with the negative temperature anomalies and sharp inversion layer over the cloud-top layer of the TCs. This demonstrates the feasibility of the perturbation approaches used in this study. However, while the bending angle always shows a consistent anomaly at the cloud top level, the temperature is sometimes less sensitive (especially for the lower vertical resolution of RAOB measurements), so that the GPS bending angle approach is best suited for the cloud top detection.

[47] The cold temperature anomaly and strong inversion at cloud top observed for TCs is similar to the behavior identified for intense convective clouds using GPS data in Biondi12. The GPS and radiosonde data furthermore show

an anomalously warm upper troposphere for TCs, which is a well-known feature [e.g., Emanuel, 1986]; this behavior was not observed for the convective systems studied in Biondi12. The cloud-top lapse rate structure in TCs (Figure 13) is similar to that for deep convection (Figure 9 of Biondi12), approaching a moist adiabat, and this is suggestive of rapid undiluted ascent as a mechanism for the large-scale cold anomaly near cloud top.

[48] The accuracy of TC cloud-top height depends to some degree on the proper representative of background bending angle and temperature climatologies. To further quantify the uncertainty of the derived TC cloud-top heights due to the representation of the background bending angle and temperature climatologies, we recalculated all of the RO bending angle anomalies using the monthly mean and the annual mean climatologies, respectively. We found (not shown) that the RO-derived cloud-top heights are nearly identical using either a monthly mean, an annual mean, or the multiyear mean climatology. When the cloud-top height is far enough from the tropopause level, the anomaly profiles often show two local minima for temperature (and two local maxima for bending angle), where the lower one corresponds to the top of the cloud (verified by the CALIOP measurements) and the higher one corresponds to the tropopause. This is consistent with the findings in Biondi2012, studying CS and CC cloud-top heights.

[49] Comparing the RO profiles with independent measurements (i.e., RAOBs and CALIOP), we need to consider some issues that could lead to errors and misinterpretations. The temporal and spatial mismatches between the RO data and the RAOB/CALIOP measurements are responsible for part of the differences in the comparisons of the cloud-top heights, especially when TCs are rapidly changing their vertical and horizontal structure. Additionally, the horizontal resolution of the limb-viewing RO measurements [Kursinski et al., 1997] is about 250 km in the UTLS, where the nadir-viewing CALIOP footprint is about 88 m in diameter. Despite the errors of representation between the RO and CALIOP measurements, the root-mean-square error of the cloud-top height difference is as small as 365 m (for the subset of 13 cases where RO and CALIOP measurements are within 2 h and 100 km). These comparison results give us confidence in the TC cloud-top height determination algorithm based on RO data.

[50] As mentioned in section 2, the GPS RO bending angle is related to atmospheric refractivity, which is a function of the temperature, water vapor, and pressure. During the TCs, strong convection leads to a possible increase of the water vapor amount in the midtroposphere and sometimes in the lower stratosphere due to the water vapor overshooting [Romps and Kuang, 2009]. Randel and Park [2006] showed that the enhanced water vapor in the upper troposphere during strong convection events can be as large as a few hundred ppmv, which, in some extreme cases, could affect the refractivity and bending angle anomalies. The water vapor overshooting effect on the top of the cloud layer may introduce positive cloud-top height bias up to a few hundred meters compared to the cloud-top heights determined by temperature profiles (i.e., Nakri, 31 May 2008), even though the cloud-top heights detected by bending angle anomalies are very close to those from temperature anomalies as demonstrated from those 34 RO-CALIOP pairs and 246 RO-RAOB pairs used in this study.

[51] In addition, gravity waves can also be found at the top of the storms [Ming et al., 2010], which may affect the estimate of the cloud-top height by using the perturbation method introduced in this study. To verify whether the temperature (and bending angle) anomalies at the top of the clouds are affected by gravity waves, we would need a large number of RO observations in a large area around the storm for an extended period of time to detect the propagation of gravity waves in space and time.

[52] A possible future application of the cloud-top height detection method presented in this study could be to probe the same storm at different stages and link the cloud-top height to the intensity of the storm as suggested by Wong and Emanuel [2007]. Currently, more than 10 years of RO data from multiple RO missions, such as CHAMP, COSMIC, GRACE, and Metop-A, are available, and more RO missions have recently launched (such as Satelite de Aplicaciones Cientificas-D, OceanSat-2, and Metop-B) or are planned for the near future. For example, the Atomic Clock Ensemble in Space, on board the International Space Station, promises to increase the number of tropical RO soundings in the near future and the COSMIC-2 program will launch six new satellites into low-inclination orbits in early 2016, and another six satellites into high-inclination orbits in early 2018. Additionally, the evolving European navigation system, Galileo, will substantially increase the number of GPS transmitters and resulting occultations. Thus, over the next decade, an increasing number of RO data will become available and can be used to study the evolution of the cloud-top height in TCs and different convection systems, and improve our understanding of the physical mechanisms that control these systems.

References

Aberson, S. D., M. L. Black, R. A. Black, J. J. Cione, C. W. Landsea, F. D. Marks, and R. W. Burpee (2006), Thirty years of tropical cyclone research with the NOAA P-3 aircraft, *Bull. Am. Meteor. Soc.*, *87*, 1039–1055, doi:10.1175/BAMS-87-8-1039.

Anthes, R. A., et al. (2008), The COSMIC/Formosat-3 mission: Early results, *Bull. Am. Meteor. Soc.*, *89*, 313–333.

Beyerle, G., T. Schmidt, G. Michalak, S. Heise, J. Wickert, and C. Reigber (2005), GPS radio occultation with GRACE: Atmospheric profiling utilizing the zero difference technique, *Geophys. Res. Lett.*, *32*, L13806, doi:10.1029/2005GL023109.

Biondi, R., W. Randel, S. P. Ho, T. Neubert, and S. Syndergaard (2012), Thermal structure of intense convective clouds derived from GPS radio occultations, *Atmos. Chem. Phys*, *12*, 5309–5318, doi:10.5194/acp-12-5309-2012.

Brueske, K. F., and C. S. Velden (2003), Satellite based tropical cyclone intensity estimation using the NOAA-KLM series Advanced Microwave Sounding Unit (AMSU), *Mon. Weather Rev.*, *131*(4), 687–697.

Chaboureau, J.-P., J.-P. Cammas, J. Duron, P. J. Mascart, N. M. Sitnikov, and H.-J. Voessing (2007), A numerical study of tropical cross-tropopause transport by convective overshoots, *Atmos. Chem. Phys.*, *7*, 1731–1740.

Chang, F. L., P. Minnis, J. K. Ayers, M. J. McGill, R. Palikonda, D. A. Spangenberg, W. L. Smith Jr., and C. R. Yost (2010), Evaluation of satellite-based upper troposphere cloud top height retrievals in multi-layer cloud conditions during TC4, *J. Geophys. Res.*, *115*, D00J05, doi:10.1029/2009JD013305.

Corti, T., et al. (2008), Unprecedented evidence for overshooting convection hydrating the tropical stratosphere, *Geophys. Res. Lett.*, *35*, L10810, doi:10.1029/2008GL033641.

Demuth, J. L., M. DeMaria, and T. H. Vonder Haar (2004), Evaluation of Advanced Microwave Sounding Unit tropical-cyclone intensity and size estimation algorithm, *J. Appl. Meteorol.*, *43*(2), 282–296.

Dvorak, V. F. (1975), Tropical cyclone intensity analysis and forecasting from satellite imagery, *Mon. Weather Rev.*, *103*(5), 420–430.

Emanuel, K. A. (1986), An Air-Sea Interaction Theory for Tropical Cyclones Part I: Steady-State Maintenance, *J. Atmos. Sci.*, *43*, 585–605.

Emanuel, K. A. (1999), Thermodynamic control of hurricane intensity, *Nature*, *401*, 665–669.

Fjeldbo, G., A. J. Kliore, and V. R. Eshleman (1971), The neutral atmosphere of Venus as studied with the Mariner V radio occultation experiments, *Astron. J.*, *76*, 123–140.

Foelsche, U., B. Scherllin-Pirscher, F. Ladstaedter, A. K. Steiner and G. Kirchengast (2011), Refractivity and temperature climate records from multiple radio occultation satellites consistent within 0.05%, *Atmos. Meas. Tech.*, *4*, 2007–2018, doi:10.5194/amt-4-2007-2011.

Grosvenor, D. P., T. W. Choularton, H. Coe, and G. Held (2007), A study of the effect of overshooting deep convection on the water content of the TTL and lower stratosphere from Cloud Resolving Model simulations, *Atmos. Chem. Phys.*, *7*, 4977–5002, doi:10.5194/acp-7-4977-2007.

Hajj, G. A., C. O. Ao, B. A. Iijima, D. Kuang, E. R. Kursinski, A. J. Mannucci, T. K. Meehan, L. J. Romans, M. de La Torre Juarez, and T. P. Yunck (2004), CHAMP and SAC-C atmospheric occultation results and intercomparisons, *J. Geophys. Res.*, *109*, D06109, doi:10.1029/2003JD003909.

Ho, S.-P., et al. (2009a), Estimating the uncertainty of using GPS radio occultation data for climate monitoring: Inter-comparison of CHAMP refractivity climate records 2002–2006 from different data centers, *J. Geophys. Res.*, *114*, D23107, doi:10.1029/2009JD011969.

Ho, S.-P., M. Goldberg, Y.-H. Kuo, C.-Z. Zou, and W. Schreiner (2009b), Calibration of temperature in the lower stratosphere from microwave measurements using COSMIC radio occultation data: Preliminary results, *Terr. Atmos. Oceanic Sci.*, *20*, doi:10.3319/TAO.2007.12.06.01(F3C).

Ho, S.-P., Y.-H. Kuo, W. Schreiner, and X. Zhou (2010), Using SI-traceable Global Positioning System radio occultation measurements for climate monitoring [In "States of the Climate in 2009], *Bul. Am. Meteor. Soc.*, *91*(7), S36–S37.

Ho, S.-P., et al. (2012), Reproducibility of GPS radio occultation data for climate monitoring: Profile-to-profile inter-comparison of CHAMP climate records 2002 to 2008 from six data centers, *J. Geophys. Res.*, *117*, D18111, doi:10.1029/2012JD017665.

Holz, R. E., S. Ackerman, P. Antonelli, F. Nagle, R. O. Knuteson, M. McGill, D. L. Hlavka, and W. D. Hart (2006), An improvement to the high-spectral-resolution CO2-slicing cloud-top altitude retrieval, *J. Atmos. Oceanic Technol.*, *23*, 653–670, doi:10.1175/JTECH1877.1.

Jarvinen, B. R., C. J. Neumann, and M. A. S. Davis (1984), A Tropical cyclone data tape for the North Atlantic basin, 1886–1983: Contents, limitations, and uses, NOAA Technical Memorandum NWS NHC 25.

Jensen, E., L. Pfister, T. Bui, A. Weinheimer, E. Weinstock, J. Smith, J. Pittman, D. Baumgardner, P. Lawson, and M. J. McGill (2005), Formation of a tropopause cirrus layer observed over Florida during CRYSTAL-FACE, *J. Geophys. Res.*, *110*, D03208, doi:10.1029/2004JD004671.

Kidder, S. Q., W. M. Gary, and T. H. Vonder Haar (1978), Estimating tropical cyclone central pressure and outer winds from satellite microwave data, *Mon. Weather Rev.*, *106*(10), 1458–1464.

Kidder, S. Q., M. D. Goldberg, R. M. Zehr, M. DeMaria, J. F. W. Purdom, C. S. Velden, C. C. Goody, and S. J. Kusselson (2000), Satellite analysis of tropical cyclones using the Advanced Microwave Sounding Unit (AMSU), *Bull. Am. Meteor. Soc.*, *81*, 1241–1260.

King, M. D., Y. J. Kaufman, W. P. Menzel, and D. Tanre (1992), Remote sensing of cloud, aerosol and water vapor properties from the moderate resolution imaging spectrometer (MODIS), *IEEE Trans. Geosci. Remote Sens.*, *30*, 2–27.

Knibbe, W. J. J., J. F. de Haan, J. W. Hovenier, D. M. Stam, R. B. A. Koelemeijer, and P. Stammes (2000), Deriving terrestrial cloud top pressure from photopolarimetry of reflected light, *J. Quant. Spectrosc. Radiat. Transfer.*, *64*, 173–199.

Koelemeijer, R. B. A., P. Stammes, J. W. Hovenier, and J. F. de Haan (2002), Global distributions of effective cloud fraction and cloud top pressure derived from oxygen A band spectra measured by the global ozone monitoring experiment: Comparison to ISCCP data, *J. Geophys. Res.*, *107*(D12), 4151, doi:10.1029/2001JD000840.

Kuo, Y. H., T. K. Wee, S. Sokolovskiy, C. Rocken, W. Schreiner, D. Hunt, and R. A. Anthes (2004), Inversion and error analysis of GPS radio occultation data, *J. Meteorol. Soc. Japan*, *82*, 507–531.

Kursinski, E. R., G. A. Hajj, J. T. Schofield, R. P. Linfield, and K. R. Hardy (1997), Observing Earth's atmosphere with radio occultation

measurements using the Global Positioning System, *J. Geophys. Res.*, *102*(D19), 23,429–23,465.

Luo, Z., G. L. Stephens, K. A. Emanuel, D. G. Vane, N. D. Tourville, and J. M. Haynes (2008), On the use of CloudSat and MODIS data for estimating hurricane intensity, *IEEE Geosci. Remote Sens. Lett.*, *5*, 13–16.

McGill, M. J., L. Li, W. D. Hart, G. M. Heymsfield, D. L. Hlavka, P. E. Racette, L. Tian, M. A. Vaughan, and D. M. Winker (2004), Combined lidar radar remote sensing: Initial results from CRYSTALFACE, *J. Geophys. Res.*, *109*, D07203, doi:10.1029/2003JD004030.

McGill, M. J., M. A. Vaughan, C. R. Trepte, W. D. Hart, D. L. Hlavka, D. M. Winker, and R. Kuehn (2007), Airborne validation of spatial properties measured by the CALIPSO lidar, *J. Geophys. Res.*, *112*, D20201, doi:10.1029/2007JD008768.

Merrill, R. T. (1991), Physical retrieval of typhoon structure using passive microwave observations. Preprints, 19th Conf. On hurricanes and tropical meteorology, Miami, FL, *Am. Meteorol. Soc.*, 405–408.

Ming, F. C., Z. Chen, and F. Roux (2010), Analysis of gravity-waves produced by intense tropical cyclones, *Ann. Geophys.*, *28*, 531–547.

Minnis, P., C. R. Yost, S. Sun-Mack, and Y. Chen (2008), Estimating the top of the cloud of optically thick ice clouds from thermal infrared satellite observations using CALIPSO data, *Geophys. Res. Lett.*, *35*, L12801, doi:10.1029/2008GL033947.

Naud, C., J.-P. Muller, and E. C. Clothiaux (2002), Comparison of cloud top heights derived from MISR stereo and MODIS CO_2 slicing, *Geophys. Res. Lett.*, *29*(16), 1795, doi:10.1029/2002GL015460.

Platnick, S., M. D. King, S. A. Ackerman, W. P. Menzel, B. A. Baum, J. C. Riedi, and R. A. Frey (2003), The MODIS cloud products: Algorithms and examples from Terra, *IEEE Trans. Geosci. Remote Sens.*, *41*, 459–473.

Poole, L. R., D. M. Winker, J. R. Pelon, and M. P. McCormick (2002), CALIPSO: GLOBAL aerosol and cloud observations from lidar and passive instruments, *Proc. SPIE*, *481*, 419–426.

Prata A. J., and P. J. Turner (1997), Cloud-top height determination using ATSR data, *Remote Sens. Environ.*, *59*, 1–13.

Randel, W. J., and M. Park (2006), Deep convective influence on the Asian summer monsoon anticyclone and associated tracer variability observed with Atmospheric Infrared Sounder (AIRS), *J. Geophys. Res.*, *111*, D12314, doi:10.1029/2005JD006490.

Rodger, C. J., J. B. Brundell, and R. L. Dowden (2005), Location accuracy of VLF World Wide Lightning Location (WWLL) network: Post-algorithm upgrade, *Ann. Geophys.*, *23*, 277–290.

Romps, D. M., and Z. Kuang (2009), Overshooting convection in tropical cyclones, *Geophys. Res. Lett.*,. *36*, L09804, doi:10.1029/2009GL037396.

Rossow, W. B., and R. A. Schiffer (1999), Advances in understanding clouds from ISCCP, *Bull. Am. Meteorol. Soc.*, *80*, 2261–2288.

Rozanov, V. V., A. A. Kokhanovsky, and J. P. Burrows (2004), The determination of cloud altitudes using GOME reflectance spectra: multilayered cloud systems, *IEEE Trans. Geosci. Remote Sens.*, *42*, 1009–1017.

Schmetz, J., S. A. Tjembs, M. Gube, and L. Van de Berg (1997), Monitoring deep convection and convective overshooting with Meteosat, *Adv. Space Res.*, *19*, 433–441.

Schreiner, W., C. Rocken, S. Sokolovskiy, S. Syndergaard, and D. Hunt (2007), Estimates of the precision of GPS radio occultations from the COSMIC/FORMOSAT-3 mission, *Geophys. Res. Lett.*, *34*, L04808, doi:10.1029/2006GL027557.

Sherwood, S. C., T. Horinouchi, and H. A. Zeleznik (2003), Convective impact on temperatures observed near the tropical tropopause, *J. Atmos. Sci.*, *60*, 1847–1856.

Sherwood, S. C., P. Minnis, M. McGill, and J. C. Chae (2004), Underestimation of deep convective cloud tops by thermal imagery, *Geophys. Res. Lett.*, *31*, L11102, doi:10.1029/2004GL019699.

Smith, E. K., and S. Weintraub (1953), The constants in the equation of atmospheric refractive index at radio frequencies, *Proc. IRE*, *41*, 1035–1037, doi:10.1109/JRPPROC.1953.274297.

Vaughan, M., S. Young, D. Winker, K. Powell, A. Omar, Z. Liu, Y. Hu, and C. Hostetler (2004), Fully automated analysis of space-based lidar data: An overview of the CALIPSO retrieval algorithms and data products, *Proc. SPIE Int. Soc. Opt. Eng.*, *5575*, 16–30.

Velden C. S., et al. (2006), The Dvorak tropical cyclone intensity estimation technique: A satellite-based method that has endured for over 30 years, *Bull. Am. Meteorol. Soc.*, *87*(9), 1195–1210.

Wickert, J., et al. (2001), Atmosphere sounding by GPS radio occultation: First results from CHAMP, *Geophys. Res. Lett.*, *28*(17), 3263–3266.

Winker, D. M., W. H. Hunt, and M. J. McGill (2007), Initial performance assessment of CALIOP, *Geophys. Res. Lett.*, *34*, L19803, doi:10.1029/2007GL030135.

Wong V., and K. A. Emanuel (2007), Use of cloud radars and radiometers for tropical cyclone intensity estimation, *Geophys. Res. Lett.*, *34*, L12811, doi:10.1029/2007GL029960.